

Quantum Fluctuations Driving the Generation and Strong Correlations of Fission Fragment Angular Momenta

M. H. Zhou¹, S. Y. Chen^{1,*}, Z. Y. Li^{2,1}, M. S. Smith³, and Z. P. Li^{1†}

¹*School of Physical Science and Technology, Southwest University, Chongqing 400715, China*

²*China Nuclear Data Center, China Institute of Atomic Energy, Beijing 102413, China*

³*Physics Division, Oak Ridge National Laboratory, Oak Ridge, Tennessee, 37831-6354, USA*

(Dated: March 12, 2024)

Two critical issues in the study of the fission mechanism are how the fission fragment angular momenta (FFAM) develop dynamically from equilibrium and how they are correlated with each other. To this end, we construct a time-dependent generator coordinate method that incorporates crucial quantum fluctuations – multiple rotations, vibrations, and their couplings – based on covariant density functional theory, providing for the first time a global, microscopic, and dynamical study on the FFAM distribution. The calculated probability distributions of FFAM are in good agreement with the experimental measurements, and the sawtooth-like mass dependence of average FFAM is reproduced very well. It is noteworthy to find that the quantum fluctuations drive the generation and chaotic evolution of FFAM during fission fragment formation and induce the strong correlations of FFAM orientations at the small, medium, and large opening angles ($\phi_{\text{LH}} \approx 30^\circ, 90^\circ, 160^\circ$).

Introduction.—Insights into the generation and evolution of fission fragment angular momenta (FFAM) are not only important for a fundamental understanding of the fission mechanism, but also have implications for a number of key issues during the deexcitation process, such as the anisotropy of neutron emission [1, 2], γ -ray multiplicity and angular distributions [3–6], the γ -ray heating problem in nuclear reactors [7], and more. Since the 1960s, significant efforts have been invested in the experimental measurement of FFAM [8–13], culminating with an impressive advance by Wilson *et al.* in 2021 [14]: a sawtooth-like mass dependence of FFAM with high precision was measured across three different fission reactions. The observed lack of correlation between the angular momenta of the fragment partners was interpreted as evidence of their postscission origin, which triggered vigorous discussions in the literature on the generation, dynamics, and correlations of FFAM [15–28].

Theoretical studies on the mechanism of FFAM are mainly based on models that include statistical fluctuations and/or quantum effects [5, 26–30] and the angular momentum projection on a microscopic static/dynamic intrinsic wave function [15–17, 31, 32]. Very recently, a time-dependent collective Hamiltonian model was proposed to analyze the dynamics of FFAM during and after scission in a scheme including multiple rotations [18]. These methods can essentially reproduce the distribu-

tions of FFAM and demonstrate the significance of the quantum effects and quantum fluctuations. However, the crucial and challenging issue of how FFAM develop dynamically from equilibrium is still not understood, especially within a microscopic framework. Moreover, the impact of quantum fluctuations on correlations between FFAM distributions needs further investigation. Clearly, these require a global, dynamical, and microscopic study that can describe the generation and evolution of FFAM throughout the entire fission process and includes descriptions of as many quantum fluctuations as possible.

Here, we construct a time-dependent generator coordinate method that incorporates multiple rotations of fragments and the relative motion, vibrations, and couplings between them in a large collective space based on the microscopic covariant density functional theory (CDFT), which is referred to as TD-MRV. We investigate the generation and continuous evolution of FFAM from the equilibrium state of the compound nucleus to a large separation of fission fragments for the first time, and analyze the correlations of FFAM with quantum fluctuations.

Theoretical Model.—Low-energy nuclear fission is a slow and large-amplitude collective motion involving complex quantum fluctuations in a series of collective degrees of freedom. The quantum fluctuations mainly manifest as shape vibrations, and can also induce collective rotations especially when the nucleus goes beyond the saddle point, where the elongation of the compound nucleus accelerates and the fragments are forming [33]. As the nucleus further elongates, the collective rotations will gradually converge to those of the

* S. Y. Chen’s contribution is equal to M. H. Zhou’s in this work and should be considered as co-first authors

† E-mail: zpliphy@swu.edu.cn

two forming fragments and the relative rotation between them. Figure 1 shows a schematic picture of the collective vibrations, rotations, and their combinations within a fissioning nucleus, which can be regarded as quantum fluctuations of the mass multipole moments (shapes of compound nucleus and fragments). These collective rotations are coupled to each other by the multipole-multipole interactions and the dominant part is the quadrupole-quadrupole interaction [34].

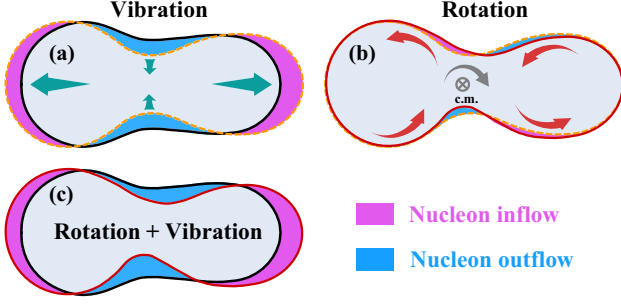


FIG. 1. Scheme of the collective vibrations (a), rotations (b), and their combinations (c) of a fissioning nucleus caused by quantum fluctuations.

To this end, we can construct a collective Hamiltonian that includes not only vibrations in axially symmetric quadrupole and octupole shapes β_2 and β_3 , but also the rotations of two (forming) fragments and their relative motion:

$$\hat{H} = -\frac{\hbar^2}{2} \sum_{p,q=2,3} \frac{\partial}{\partial \beta_p} B_{pq}^{-1} \frac{\partial}{\partial \beta_q} + \sum_i \frac{\hat{S}_i^2}{2\mathcal{I}_i} + V(\beta_2, \beta_3) + \sum_{i<j} \chi_2 \hat{Q}_2^i \cdot \hat{Q}_2^j, \quad (i, j = L, H, \Lambda) \quad (1)$$

where B_{pq} and V are the collective masses and potential, respectively. $S_{L(H)}$ is the angular momentum of the light (heavy) fragment and S_Λ is the relative orbital angular momentum between two fragments. $\mathcal{I}_{L(H)}$ and \mathcal{I}_Λ are the corresponding moments of inertia. Before the onset

of fission fragments, the rotations reduce to the one of the mother nucleus described by the \hat{S}_Λ term. χ_2 in the quadrupole-quadrupole interaction terms denotes the interaction strength. \hat{Q}_2^i is the quadrupole operator that is related to the intrinsic quadrupole deformation β_2^i [35].

In this work, the deformation-dependent collective masses B_{pq} , moments of inertia \mathcal{I}_i , collective potential V , and quadrupole deformations of fragments $\beta_2^{L,H}$ are all determined microscopically by the CDFT with constraints on the quadrupole and octupole deformations for the configurations inside the scission line and constraints on the density distributions with frozen fragments for the configurations beyond scission [36]. The detailed expressions for the collective parameters can be found in our previous work [37, 38]. It is noteworthy that the $\mathcal{I}_{L(H)}$ is also calculated using the Inglis-Beliaev formula [39, 40] based on the intrinsic mean-field potential of the fragment, which is deduced from its density distribution under the same CDFT framework (*c.f.* Fig. S1 [41]).

Then, we can simulate the fission dynamics and, in particular, the generation and continuous evolution of FFAM by performing the time evolution of a collective wave function, which takes the form

$$\sum_n \phi_n(\beta_2, \beta_3, t) |S_{LH} S_{LH} S_\Lambda; JM\rangle, \quad (2)$$

$$n \equiv (S_L, S_H, S_\Lambda)$$

for a certain total angular momentum J . ϕ_n is the wave packet in the collective space of shapes and n labels the different angular momentum coupling channels. Here, J is set to zero following the previous works [18, 27, 28, 42], and meanwhile, we reduce the two-dimensional collective space (β_2, β_3) to a certain path with the variable β ($\delta\beta = \sqrt{\delta\beta_2^2 + \delta\beta_3^2}$) due to a fact that the collective currents in the (β_2, β_3) plane mainly flow over the optimal fission valley (*c.f.* Fig. S2 and video [41]). Finally, we obtain a time-dependent coupled channel Schrödinger-like equation:

$$i\hbar \frac{\partial}{\partial t} \phi_n(\beta, t) = \left[-\frac{\hbar^2}{2} \frac{\partial}{\partial \beta} B^{-1}(\beta) \frac{\partial}{\partial \beta} + \sum_i \frac{S_i(S_i + 1)\hbar^2}{2\mathcal{I}_i} + V(\beta) \right] \phi_n(\beta, t) + \sum_{i<j} \sum_{n' \neq n} \Gamma_{nn'}^{ij} \phi_{n'}(\beta, t) \quad (3)$$

with

$$\Gamma_{nn'}^{ij} = \chi_2 (-1)^{S'_i + S'_j + S'_k} \begin{Bmatrix} S'_i & 2 & S_i \\ S_j & S'_k & S'_j \end{Bmatrix} \langle S_i || \hat{Q}_2^i || S'_i \rangle \times \langle S_j || \hat{Q}_2^j || S'_j \rangle \delta_{S_k S'_k}, \quad (k \neq i \neq j). \quad (4)$$

It is solved numerically based on a finite difference method in the collective space and the Crank-Nicolson scheme for time integration [43]. The initial state is made by boosting the static ground state along the β -path to an excitation energy 1 MeV higher than the

inner fission barrier and the angular momenta satisfy $J = S_L = S_H = S_\Lambda = 0$. As the fission fragments are forming, the angular momenta S_L, S_H, S_Λ are generated gradually by the descending collective potential and quadrupole-quadrupole interactions. The average rotational energy during the fission process is kept $\lesssim 1$ MeV. The angular momenta obey triangular rule $\Delta(S_H S_L S_\Lambda)$, and they are truncated at $36 \hbar$ for S_H , and $40 \hbar$ for S_L and S_Λ .

It is noteworthy that the quadrupole-quadrupole interactions play a crucial role in the dynamics of FFAM. In principle, the interaction strength χ_2 can be extracted approximately by determining constraints on the quadrupole deformations of the fragments based on CDFT. However, in order to show the effect of the interactions on the generation and evolution of FFAM more clearly, we use a Fermi formulation for χ_2 as

$$\chi_2 = \frac{c}{1 + \exp[(\beta - \beta_0)/\Delta\beta]} \quad (5)$$

where β_0 is the point beyond scission where the fragments are separated by 0.5 fm [18], and $\Delta\beta = 2(\beta_0 - \beta_{\text{scission}})/4.4$. Clearly, χ_2 remains almost a constant c from saddle to scission and then decays rapidly, which can catch the characteristics of nuclear force well. c is determined by reproducing the pattern of experimental angular momentum distribution for a chosen heavy fragment in the Extended Data of Fig. 4 of Ref. [14]. Here, $c = 0.11$ MeV/ b^2 is used for the induced fission of ^{240}Pu .

When fragments separate far enough, which we set to be the distance between the centers of mass $d_{\text{c.m.}}^{\text{FFs}} > 23$ fm, they are fully decoupled [32], and one can calculate the probability flux for each angular momentum channel:

$$F_n = \int_{t_0}^t \mathbf{J}_n(\beta, t) dt, \quad n \equiv (S_L, S_H, S_\Lambda) \quad (6)$$

with the current

$$\begin{aligned} \mathbf{J}_n(\beta, t) \\ = \frac{\hbar}{2i} \frac{1}{B(\beta)} [\phi_n^*(\beta, t) \nabla \phi_n(\beta, t) - \phi_n(\beta, t) \nabla \phi_n^*(\beta, t)]. \end{aligned} \quad (7)$$

Finally, the two- and one-dimensional probability distributions of FFAM can be obtained by summing over the flux with respect to other component(s)

$$P(S_L, S_H) = \sum_{S_\Lambda} F_n, \quad P(S_L \text{ or } S_H) = \sum_{S_H \text{ or } S_L} P(S_L, S_H). \quad (8)$$

Results and Discussion— Here, we take ^{240}Pu as an example to analyze the generation and evolution of the FFAM. Fig. 2 (a) displays the potential energy surface (PES) in the β_2 - β_3 plane calculated by CDFT with the PC-PK1 functional [44] based on two-center harmonic oscillator basis [36]. The inner and outer fission barriers and asymmetric fission valley from $(\beta_2, \beta_3) \approx (1.3, 0.5)$ to $\approx (4.0, 2.3)$ are clearly identified, which are consistent with previous calculations using Skyrme and Gogny density functionals [45–48]. Based on the PES, the low-energy fission dynamical simulation using a time-dependent generator coordinate method [49] shows that the probability currents mainly follow the optimal fission path and its surroundings (*c.f.* Fig. S2 [41]). Therefore, we choose three fission channels around the optimal fission path: $^{134}\text{Te}+^{106}\text{Mo}$, $^{140}\text{Xe}+^{100}\text{Zr}$, and $^{150}\text{Ce}+^{90}\text{Kr}$ as examples to perform the calculations, where six fragments spread across the region of sawtooth-like distribution of FFAM [14]. The corre-

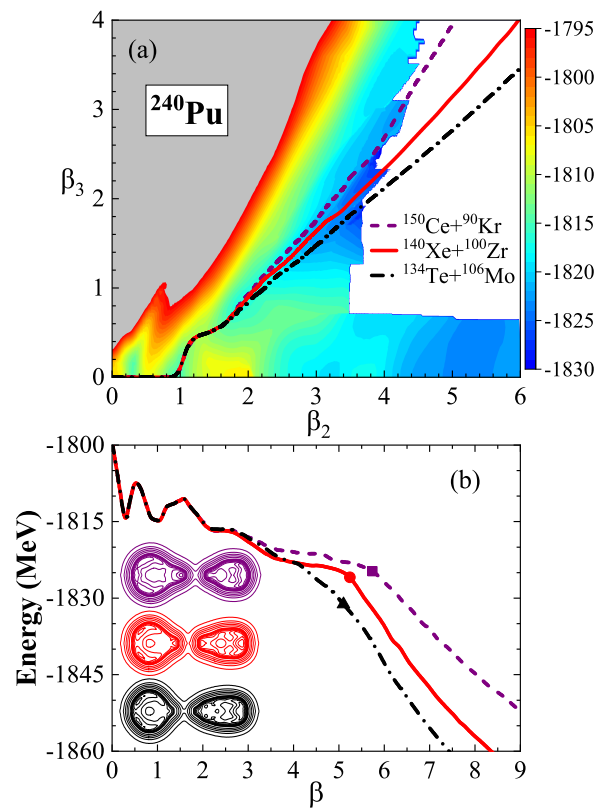


FIG. 2. (a) Potential energy surface of ^{240}Pu in the β_2 - β_3 plane calculated by CDFT with the PC-PK1 functional [44]. Three fission channels: $^{134}\text{Te}+^{106}\text{Mo}$, $^{140}\text{Xe}+^{100}\text{Zr}$, and $^{150}\text{Ce}+^{90}\text{Kr}$ are shown by the dash-dotted, solid, and dashed lines, respectively. (b) The potential energy curves and scission points (solid symbols) along the β path for the three fission channels. The corresponding scission configurations with the nucleon number in the neck $q_N = 1$ are shown.

TABLE I. The mass numbers, quadrupole deformations, and moments of inertia of the nascent fission fragments at scission.

Fragments	Mass Number (u)	β_2^i	\mathcal{I}_i (\hbar^2/MeV)
$^{134}\text{Te} (^{106}\text{Mo})$	134.19 (105.81)	0.08 (0.82)	6.30 (38.24)
$^{140}\text{Xe} (^{100}\text{Zr})$	139.80 (100.20)	0.20 (0.72)	20.20 (26.64)
$^{150}\text{Ce} (^{90}\text{Kr})$	149.53 (90.47)	0.37 (0.51)	32.08 (19.39)

sponding potential energy curves (PECs) and scission configurations are shown in Fig. 2 (b). It is noteworthy that the configurations around scission are determined in the (β_2, β_3, q_N) space [50], while the configurations beyond scission are obtained by performing density constraint calculations [36]. All the PECs drop rapidly after the outer barrier (saddle points) and then basically follow the Coulomb potential for times after scission. The fragment information at scission are summarized in Tab. I and we find that the quadrupole deformations and moments of inertia of the heavy (light) fragments increase (decrease) gradually as the mass asymmetry increases.

With all the microscopic inputs – PECs, collective masses B , moments of inertia and quadrupole deformations of the fragments (*c.f.* Figs. S3-S5 [41]) – we can simulate the dynamics of FFAM using Eq. (3). Fig. 3 displays the angular momentum distributions for the fragments along the fission path β for the channel $^{140}\text{Xe}+^{100}\text{Zr}$ as an example. The corresponding two-dimensional (2D) FFAM distributions can be found in the videos of Supplement Materials [41]. Remarkably, during fission fragment formation, *i.e.*, from the saddle point ($\beta \approx 1.7$) to scission ($\beta \approx 5.2$), we observe a rapid generation and subsequent chaotic evolution of the FFAM distribution, which are driven by the quantum fluctuations induced mainly by the sharply descending potential energy and quadrupole-quadrupole interactions. After scission, the distribution varies slightly till to a stable pattern when the fragments are well separated. Moreover, we find that the evolution of angular momentum distributions for S_L , S_H , and S_Λ [41] have similar feature.

Figs. 4 displays the final FFAM distributions and the mass dependence of the average FFAM. Extended peaks are observed in the 2D distributions (Figs. 4 (a-c)) for all three fission channels, and the peaks and entire patterns move toward to larger S_H (and lower S_L) as the mass asymmetry of the fragments increases. The corresponding 1D (Figs. 4(e-g)) distributions show this trend in projection: the peak for the heavy fragment moves from $2\hbar$ (^{134}Te) to $\sim 10\hbar$ (^{150}Ce) and the width extends dramatically, which are consistent with the measurements in the Extended Data Fig. 4 of Ref. [14].

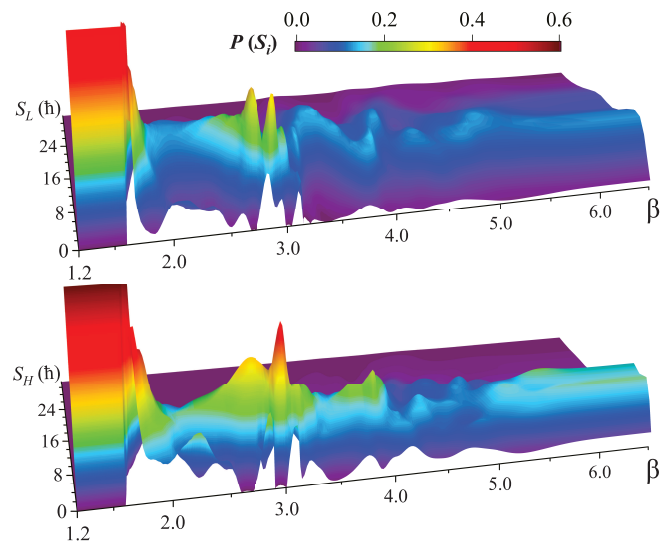


FIG. 3. Angular momentum distributions for the light (upper) and heavy (lower) fragments along the fission path for the channel $^{140}\text{Xe}+^{100}\text{Zr}$.

The distributions for S_Λ follow a similar trend as the heavy fragments, while those for light fragments are opposite. Consequently, the mass dependence of average angular momenta for the six fragments presents a clear sawtooth-like pattern, which also implies positive correlations with the quadrupole deformations and moments of inertia of the nascent fragments (*c.f.* Tab. I).

The correlations between magnitudes and orientations of FFAM are analyzed in Figs. 4 (i-l). The average angular momentum of one fragment calculated using $\langle S_i \rangle = \frac{\sum_{S'_j > S_j} S_i P(S_i, S'_j)}{\sum_{S'_j > S_j} P(S_i, S'_j)}$ varies smoothly along the cutoff S_j of the partner fragment for $S_j \leq 10\hbar$, which is in good agreement with the experimental results [14] and indicates that the magnitudes of FFAM are almost uncorrelated. However, it is remarkable to find that the distribution of orientations of FFAM described by the opening angle ϕ_{LH} [18, 26] displays strong correlations at the small, medium, and large opening angles ($\phi_{\text{LH}} \approx 30^\circ, 90^\circ, 160^\circ$). As the mass asymmetry increases, the peak at $\phi_{\text{LH}} \approx 30^\circ$ is enhanced, which is dominated by the wriggling modes (Fig. S7 [41]). The correlations differ from those given by the angular momentum projection [16] and statistical model (modified FREYA) [17], where broad peaks at $\phi_{\text{LH}} \approx 120^\circ$ and 90° are predicted. We note that the quantum fluctuations were not considered in those models. Such anisotropic correlations of FFAM can manifest themselves in the correlation between γ transitions emitted from two fragments, as reported in Ref. [51], where a hint for the enhancement of near aligned or antialigned $\gamma\gamma$ emission was

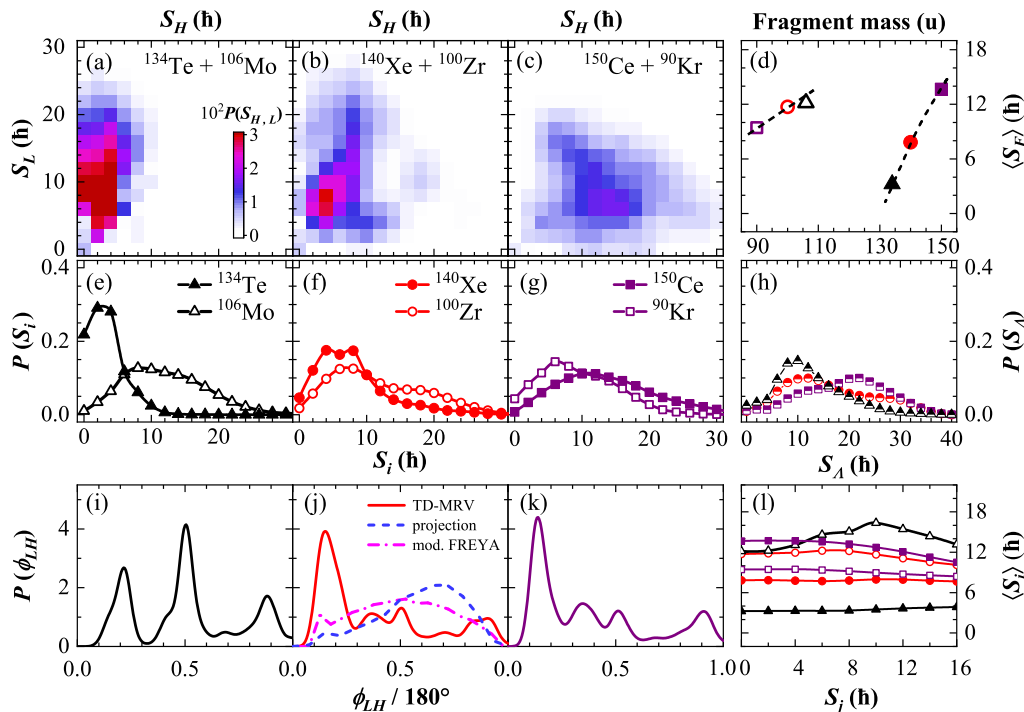


FIG. 4. The 2D (a-c) and 1D (e-g) probability distributions of FFAM for three fission channels of ^{240}Pu . (d) Mass dependence of average angular momenta for six fragments. The dashed lines are used to guide eyes. (h) The probability distributions of the relative orbital angular momentum S_A for the three fission channels. (i-k) The opening angle distributions smoothed by Gaussian convolution with $\sigma = 5^\circ$ (solid line) for the three fission channels calculated by TD-MRV. The results from angular momentum projection (dashed line) [16] and modified FREYA (dash-dotted line) [17] are also shown in panel (j). (l) Average angular momentum of one fragment as a function of the cutoff angular momentum S_j of the partner fragment.

observed. Further experimental studies are expected to provide quantitative evaluations on the calculated opening angles, and the predicted dependence on the mass asymmetry.

Summary and outlook.—We have constructed a TD-MRV model that includes multiple rotations of fragments and their relative motion, vibrations, and the couplings between them based on CDFT. We investigate the generation and evolution of FFAM from the equilibrium state of the compound nucleus to a large separation of fission fragments in a microscopic framework for the first time. The calculated probability distributions of FFAM are consistent with the experimental measurements and the sawtooth-like mass dependence of average FFAM is reproduced very well. Here, we emphasize the uniqueness of our predictions of quantum fluctuations driving the generation, chaotic evolution, and strong correlations of FFAM. Experiments on the cor-

relation between γ transitions emitted from two fission fragments are expected to provide quantitative evaluations on the predicted correlations of FFAM orientations, which could demonstrate the effect of quantum fluctuations. Finally, the microscopic TD-MRV model can be extended to include higher-order multipole interactions based on two- or even multiple-dimensional potential energy surface that can describe not only the distributions of FFAM but also those of fission yields and total kinetic energies in the same footing.

Acknowledgements—Fruitful discussions with Dr. Song Guo, Dr. Longjun Wang, and Dr. Sibor Wang are gratefully acknowledged. This work was partly supported by the National Natural Science Foundation of China (Grants No. 12375126), the Fundamental Research Funds for the Central Universities, the Special Fund from China Nuclear Data Center, and by Office of Nuclear Physics in the U.S. Dept. of Energy Office.

[1] H. R. Bowman, S. G. Thompson, J. C. D. Milton, and W. J. Swiatecki, *Phys. Rev.* **126**, 2120 (1962).
 [2] A. Gavron, *Phys. Rev. C* **13**, 2562 (1976).
 [3] R. Albrecht, W. Dünneweber, G. Graw, H. Ho, S. G. Steadman, and J. P. Wurm, *Phys. Rev. Lett.* **34**, 1400 (1975).
 [4] R. A. Dayras, R. G. Stokstad, C. B. Fulmer, D. C. Hensley, M. L. Halbert, R. L. Robinson, A. H. Snell, D. G. Sarantites, L. Westerberg, and J. H. Barker, *Phys. Rev. Lett.* **42**, 697 (1979).
 [5] R. Vogt and J. Randrup, *Phys. Rev. C* **96**, 064620 (2017).

[6] N. P. Giha, S. Marin, J. A. Baker, I. E. Hernandez, K. J. Kelly, M. Devlin, J. M. O'Donnell, R. Vogt, J. Randrup, P. Talou, I. Stetcu, A. E. Lovell, O. Litaize, O. Serot, A. Chebboubi, C.-Y. Wu, S. D. Clarke, and S. A. Pozzi, *Phys. Rev. C* **107**, 014612 (2023).
 [7] G. Rimpault, D. Bernard, D. Blanchet, C. Vaglio-Gaudard, S. Ravaux, A., and Santamarina, *Phys. Procedia* **31**, 3 (2012).
 [8] S. A. Johansson, *Nucl. Phys.* **60**, 378 (1964).
 [9] P. Armbruster, H. Labus, and K. Reichelt, *Z Naturforsch A* **26**, 512 (1971).

- [10] J. B. Wilhelmy, E. Cheifetz, R. C. Jared, S. G. Thompson, H. R. Bowman, and J. O. Rasmussen, *Phys. Rev. C* **5**, 2041 (1972).
- [11] F. Pleasonton, *Nucl. Phys. A* **213**, 413 (1973).
- [12] P. Glässel, R. Schmid-Fabian, D. Schwalm, D. Habs, and H. Helmolt, *Nucl. Phys. A* **502**, 315 (1989).
- [13] M. Travar, V. Piau, A. Göök, O. Litaize, J. Nikolov, A. Oberstedt, S. Oberstedt, J. Enders, M. Peck, W. Geerts, and M. Vidali, *Phys. Lett. B* **817**, 136293 (2021).
- [14] J. N. N. Wilson, D. Thisse, M. Lebois, N. Jovančević, D. Gjestvang, R. Canavan, M. Rudigier, D. Etasse, R.-B. Gerst, L. Gaudefroy, E. Adamska, P. Adsley, A. Algora, M. Babo, K. Belvedere, J. Benito, G. Benzoni, A. Blazhev, A. Boso, S. Bottoni, M. Bunce, R. Chakma, N. Cieplicka-Oryńczak, S. Courtin, M. L. Cortés, P. Davies, C. Delafosse, M. Falot, B. Fornal, L. Fraile, A. Gottardo, V. Guadilla, G. Häfner, K. Hauschild, M. Heine, C. Henrich, I. Homm, F. Ibrahim, L. W. Iskra, P. Ivanov, S. Jazrawi, A. Korgul, P. Koseoglou, T. Kröll, T. Kurtukian-Nieto, L. Le Meur, S. Leoni, J. Ljungvall, A. Lopez-Martens, R. Lozeva, I. Matea, K. Miernik, J. Nemer, S. Oberstedt, W. Paulsen, M. Piersa, Y. Popovitch, C. Porzio, L. Qi, D. Ralet, P. H. Regan, K. Rezykina, V. Sánchez-Tembleque, S. Siem, C. Schmitt, P.-A. Söderström, C. Sürder, G. Tocabens, V. Vedia, D. Verney, N. Warr, B. Wasilewska, J. Wiederhold, M. Yavahchova, F. Zeiser, and S. Ziliani, *Nature* **590**, 566 (2021).
- [15] P. Marević, N. Schunck, J. Randrup, and R. Vogt, *Phys. Rev. C* **104**, L021601 (2021).
- [16] A. Bulgac, I. Abdurrahman, K. Godbey, and I. Stetcu, *Phys. Rev. Lett.* **128**, 022501 (2022).
- [17] A. Bulgac, *Phys. Rev. C* **106**, 014624 (2022).
- [18] G. Scamps and G. Bertsch, *Phys. Rev. C* **108**, 034616 (2023).
- [19] G. Scamps, I. Abdurrahman, M. Kafker, A. Bulgac, and I. Stetcu, *Phys. Rev. C* **108**, L061602 (2023).
- [20] G. Scamps, *Phys. Rev. C* **109**, L011602 (2024).
- [21] S. Marin, I. A. Tolstukhin, N. P. Giha, F. Toveson, V. Protopopescu, and S. A. Pozzi, (2023), [arXiv:2311.14397 \[nucl-ex\]](https://arxiv.org/abs/2311.14397).
- [22] <https://indico.in2p3.fr/event/26459/>.
- [23] L. Sobotka, <https://centaur.tamu.edu/centaur-archives/>.
- [24] S. Marin, E. P. Sansevero, M. S. Okar, I. E. Hernandez, R. Vogt, J. Randrup, S. D. Clarke, V. A. Protopopescu, and S. A. Pozzi, *Phys. Rev. C* **105**, 054609 (2022).
- [25] J. Randrup, *Phys. Rev. C* **108**, 064606 (2023).
- [26] J. Randrup and R. Vogt, *Phys. Rev. Lett.* **127**, 062502 (2021).
- [27] J. Randrup, T. Dössing, and R. Vogt, *Phys. Rev. C* **106**, 014609 (2022).
- [28] J. Randrup, *Phys. Rev. C* **106**, L051601 (2022).
- [29] J. Randrup and R. Vogt, *Phys. Rev. C* **89**, 044601 (2014).
- [30] R. Vogt and J. Randrup, *Phys. Rev. C* **103**, 014610 (2021).
- [31] G. F. Bertsch, T. Kawano, and L. M. Robledo, *Phys. Rev. C* **99**, 034603 (2019).
- [32] A. Bulgac, I. Abdurrahman, S. Jin, K. Godbey, N. Schunck, and I. Stetcu, *Phys. Rev. Lett.* **126**, 142502 (2021).
- [33] C. L. Zhang, B. Schuetrumpf, and W. Nazarewicz, *Phys. Rev. C* **94**, 064323 (2016).
- [34] A. Bohr and B. R. Mottelson, *Nuclear Structure*, Vol. I (1975).
- [35] P. Ring and P. Schuck, *The Nuclear Many-Body Problem* (Springer Berlin, Heidelberg, 1980) p. 25.
- [36] Z. Y. Li, S. Y. Chen, M. H. Zhou, Y. J. Chen, and Z. P. Li, [arXiv](https://arxiv.org/abs/2309.03461), 2309.03461 (2023).
- [37] Z. P. Li, T. Nikšić, D. Vretenar, J. Meng, G. A. Lalazissis, and P. Ring, *Phys. Rev. C* **79**, 054301 (2009).
- [38] H. Tao, J. Zhao, Z. P. Li, T. Nikšić, and D. Vretenar, *Phys. Rev. C* **96**, 024319 (2017).
- [39] D. R. Inglis, *Phys. Rev.* **103**, 1786 (1956).
- [40] S. Beliaev, *Nucl. Phys.* **24**, 322 (1961).
- [41] See Supplemental Material in this article for the extraction of fission fragments and their intrinsic mean-field potentials, the evolution of the collective wave packet, the collective masses of the compound nucleus, moments of inertia and quadrupole deformations of the fission fragments, the angular momentum distributions for the relative rotation along the fission path, the angular momentum geometry, and videos, .
- [42] G. Scamps, *Phys. Rev. C* **106**, 054614 (2022).
- [43] H. Goutte, J. F. Berger, P. Casoli, and D. Gogny, *Phys. Rev. C* **71**, 024316 (2005).
- [44] P. W. Zhao, Z. P. Li, J. M. Yao, and J. Meng, *Phys. Rev. C* **82**, 054319 (2010).
- [45] D. Regnier, N. Dubray, N. Schunck, and M. Verrière, *Phys. Rev. C* **93**, 054611 (2016).
- [46] N. Schunck and L. M. Robledo, *Rep. Prog. Phys.* **79** (2016), 10.1088/0034-4885/79/11/116301.
- [47] P. Marević and N. Schunck, *Phys. Rev. Lett.* **125**, 102504 (2020).
- [48] Y.-J. Chen, Y. Su, G. Dong, L.-L. Liu, Z. Ge, and X. Wang, *Chin. Phys. C* **46**, 024103 (2022).
- [49] D. Regnier, N. Dubray, M. Verriere, and N. Schunck, *Comput. Phys. Commun.* **225**, 180 (2018).
- [50] M.-H. Zhou, Z.-Y. Li, S.-Y. Chen, Y.-J. Chen, and Z.-P. Li, *Chin. Phys. C* **47**, 064106 (2023).
- [51] A. G. Smith, G. S. Simpson, J. Billowes, P. J. Dagnall, J. L. Durell, S. J. Freeman, M. Leddy, W. R. Phillips, A. A. Roach, J. F. Smith, A. Jungclaus, K. P. Lieb, C. Teich, B. J. P. Gall, F. Hoellinger, N. Schulz, I. Ahmad, J. P. Greene, and A. Algora, *Phys. Rev. C* **60**, 064611 (1999).

Supplemental Materials

The Supplemental Materials include seven figures. Figure S1 illustrates the extraction of fission fragments and their intrinsic mean-field potentials in the CDFT framework. Figure S2 displays the evolution of the collective wave packet in the β_2 - β_3 plane. Figures S3, S4 and S5 show the collective masses of the compound nucleus, moments of inertia and quadrupole deformations of the fission fragments for the three fission channels as functions of deformation parameter β , respectively. Figure S6 shows the angular momentum distributions for the relative rotation along the fission path for the channel $^{140}\text{Xe} + ^{100}\text{Zr}$. Figure S7 shows the angular momentum geometry around the peak with opening angle $\phi_{LH} \approx 30^\circ$ for the fission channel $^{140}\text{Xe} + ^{100}\text{Zr}$.

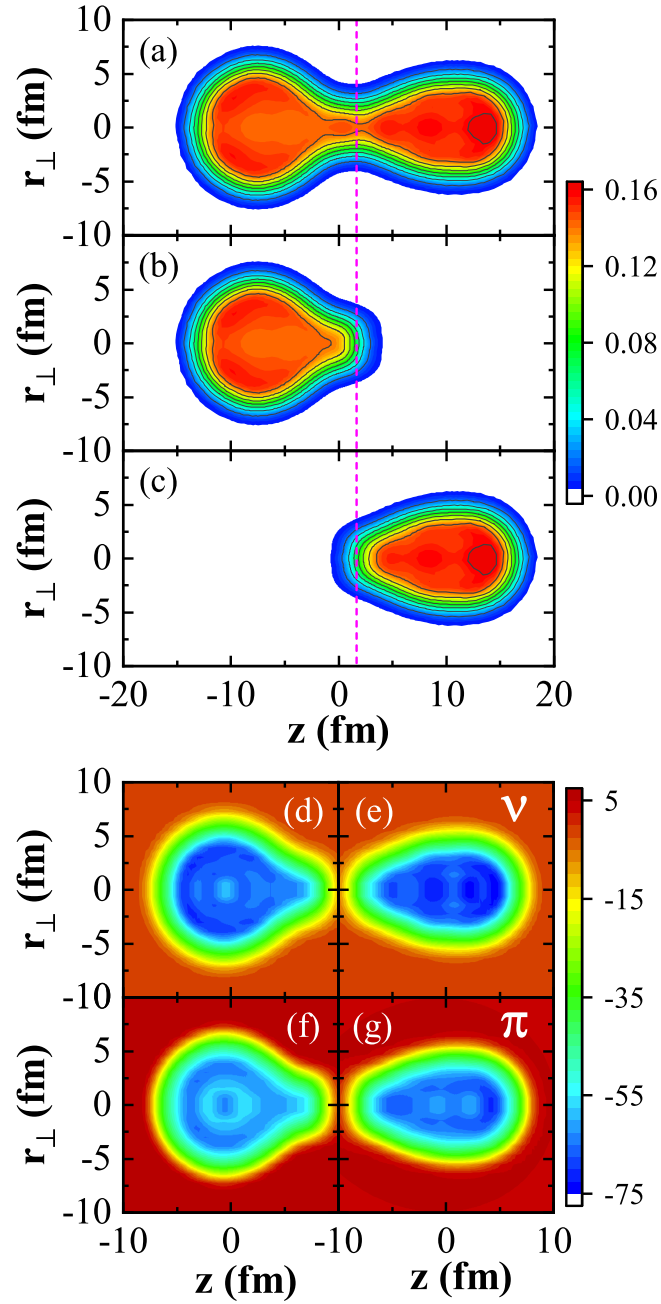


FIG. S1. (a) The nucleon density distribution at $(\beta_2, \beta_3) = (3.47, 1.91)$ of fissioning compound nucleus ^{240}Pu . (b) The density distributions for the left fission fragment extracted from that of compound nucleus using a Fermi distribution $f(z) = \frac{1}{1 + \exp[(z - z_0)/a]}$ with the neck position z_0 and diffuseness $a = 0.67$ fm. (c) Same as panel (b) but for the right fragment with a Fermi distribution $1 - f(z)$. (d-g) The neutron and proton intrinsic mean-field potentials for fission fragments determined by the corresponding densities using the same energy density functional as the whole nucleus.

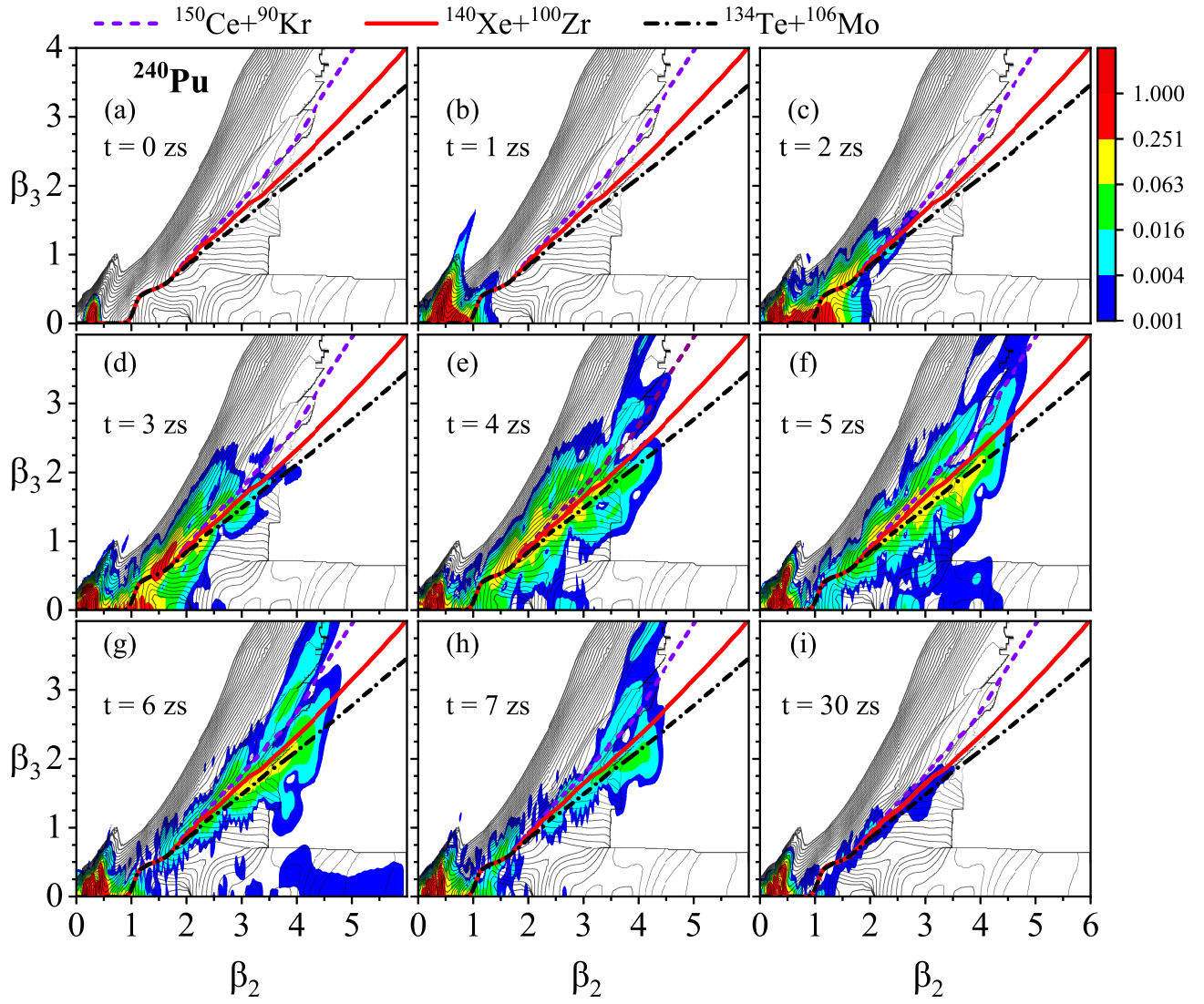


FIG. S2. Evolution of collective probability density distribution in the $\beta_2 - \beta_3$ plane for ^{240}Pu simulated by the time-dependent generator coordinate method [49].

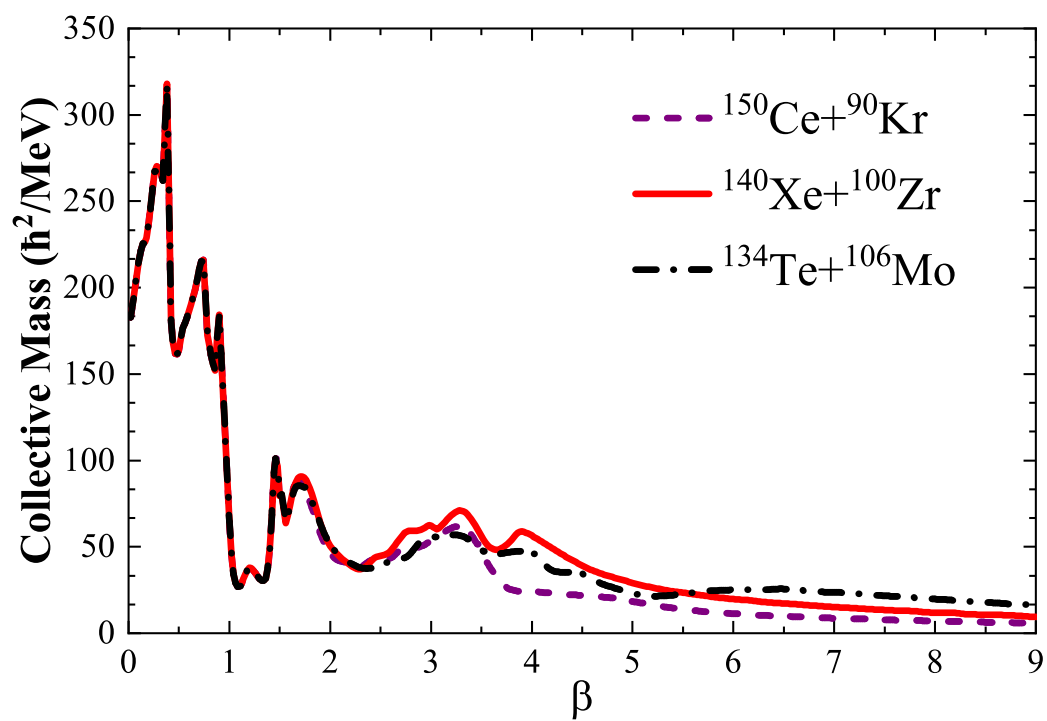


FIG. S3. The collective masses for the three fission channels as functions of β .

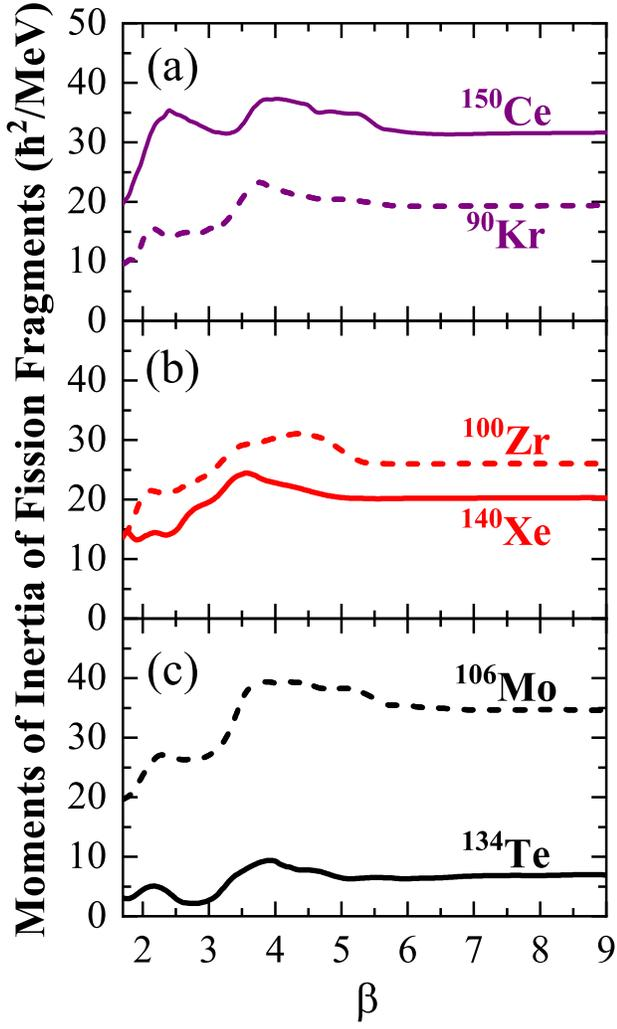


FIG. S4. Moments of inertia of fission fragments as functions of β .

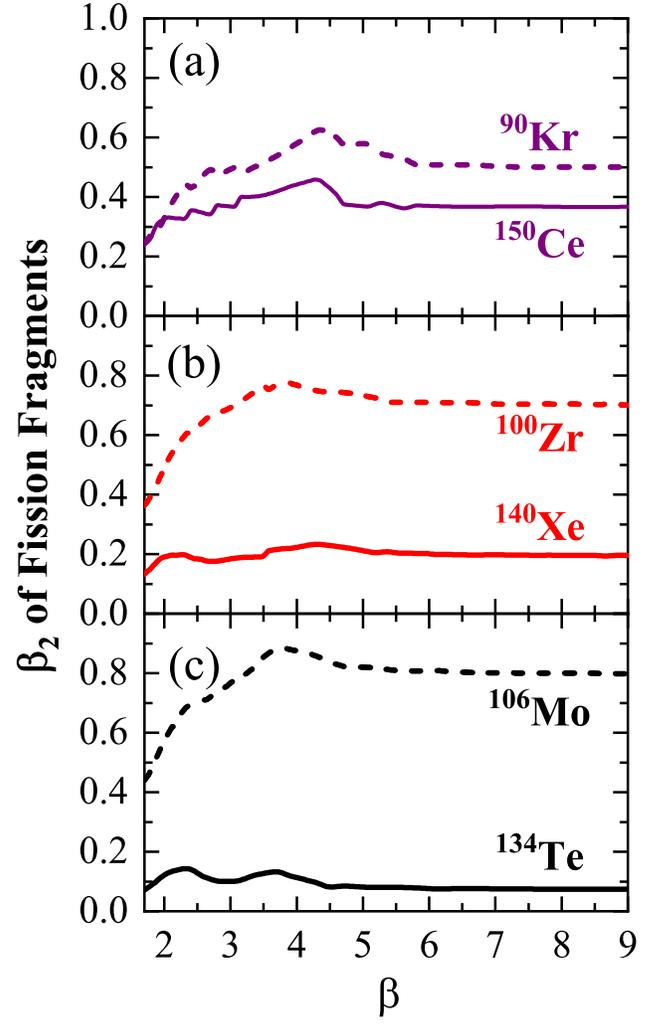


FIG. S5. Quadrupole deformations β_2 of fission fragments as functions of β .

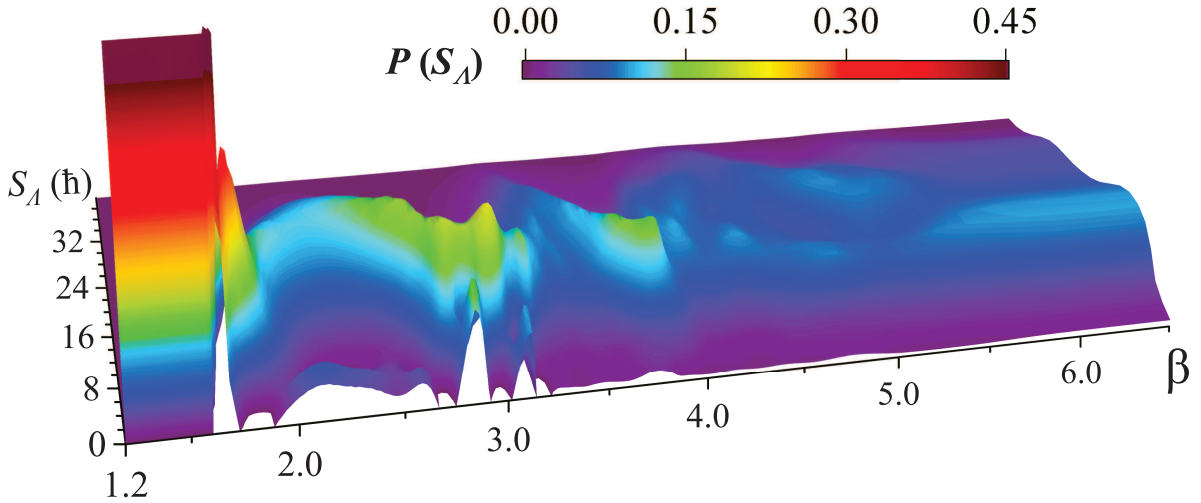


FIG. S6. Angular momentum distributions for the relative rotation between two fragments along the fission path for the channel $^{140}\text{Xe} + ^{100}\text{Zr}$.

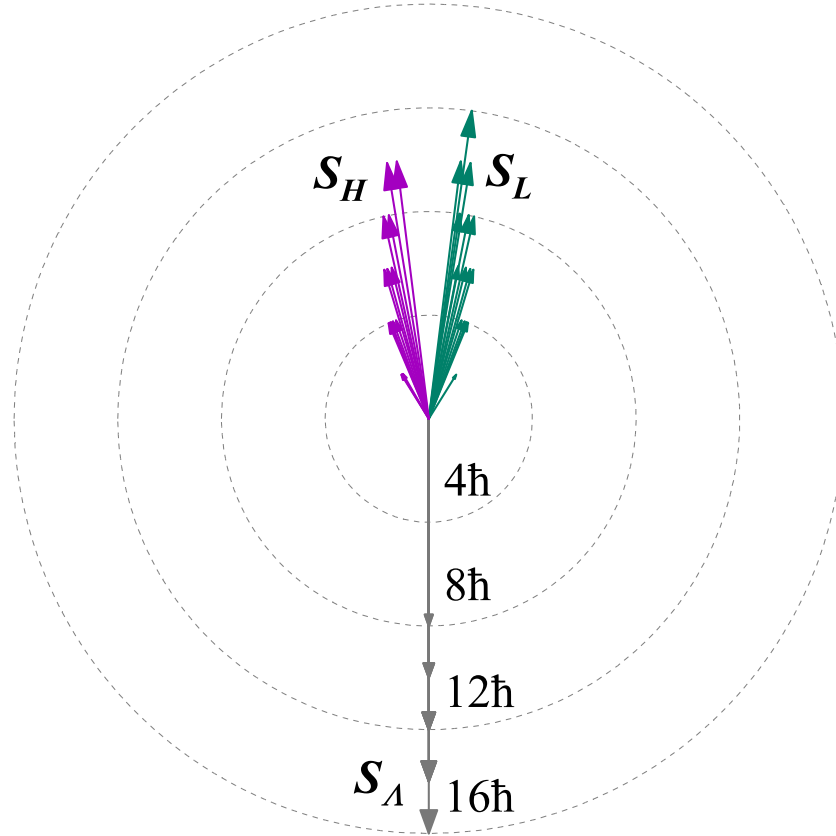


FIG. S7. The angular momentum geometry around the peak with opening angle $\phi_{LH} \approx 30^\circ$ for the fission channel $^{140}\text{Xe} + ^{100}\text{Zr}$ [c.f. Fig. 4 (j)].